Current Biology, Volume *31*

Supplemental Information

Fast tuning of posture control by visual feedback underlies gaze stabilization in walking *Drosophila*

Tomás L. Cruz, Sebastián Malagón Pérez, and M. Eugenia Chiappe

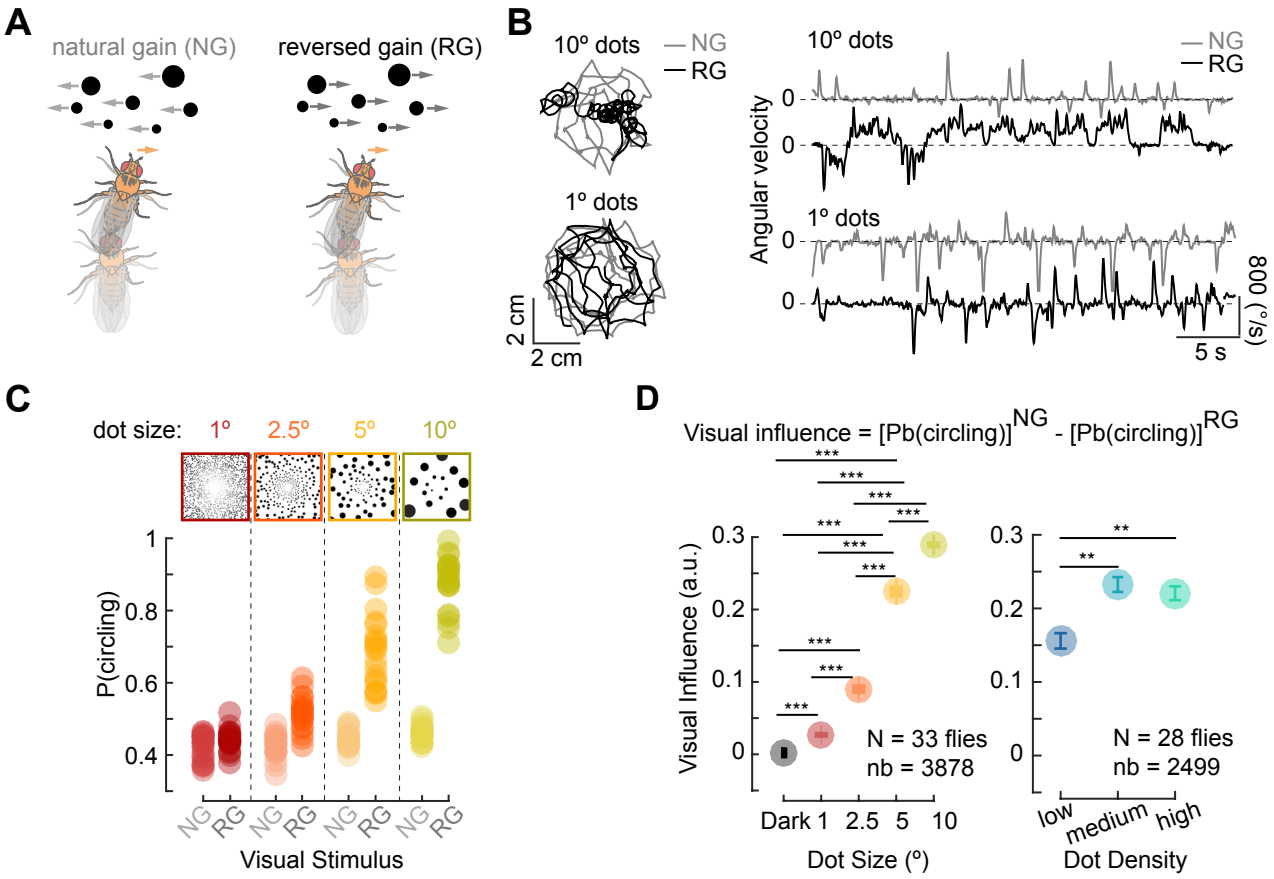

Figure S1. Visual influence over the fly's walking movements, related to Figures 1 and 4. (**A**) Visual feedback from a rightward rotation under natural (left) and reversed (right) gain conditions. (**B**) Left: example of exploratory walking paths under natural gain (light gray, NG) and reversed gain (dark gray, RG) under 10º random dots (top) and 1º random dots (bottom) visual environments. Right: corresponding angular velocity time series. (**C**) Circling probability (probability of consecutive rotations towards the same direction, see **Methods**) as a function of dot size under NG (light colors) or RG (dark colors). (**D**) Visual influence as a function of visual environments with varying dot size (left) or with varying dot density (right), MWWTest, *p<0.05, **p<0.01, ***p<0.005.

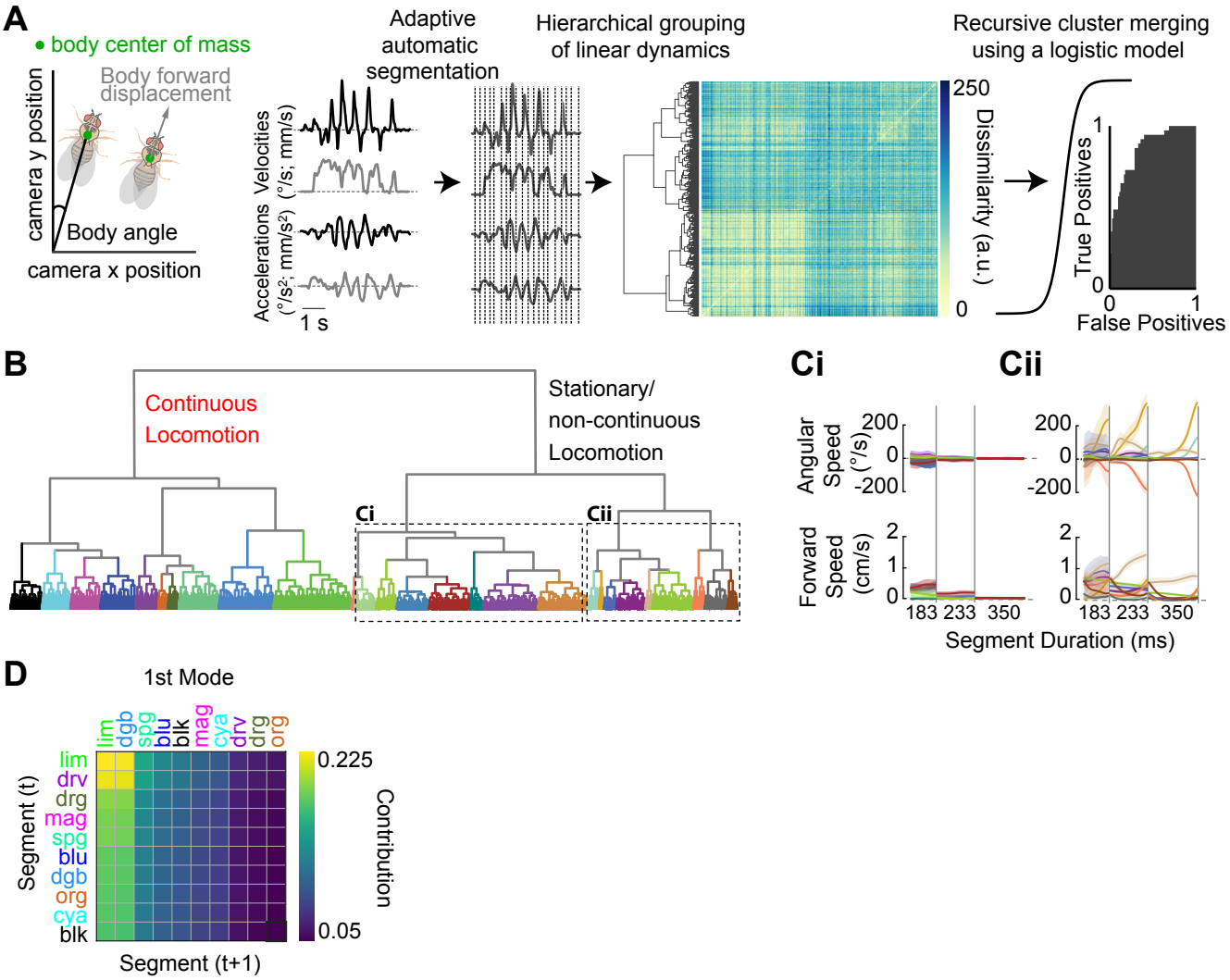

Figure S2: Unsupervised segmentation and classification of body kinematics, related to Figure 2. (**A**) Schematic of the fly's body movement. The position of the body center of mass was tracked, and the angular (black) and forward (grey) velocities and the corresponding accelerations were extracted. Using the multivariate time series defined by velocities and accelerations, the unsupervised algorithm identified temporal segments of different length. Hierarchical clustering and logistic regression analysis were applied to the segments to obtain characteristic body kinematics (see **Methods**). (**B**) Dendrogram associated with the hierarchical clustering. Note that a principled strategy was employed to select the final clusters based on their statistical separability (see **Methods**). (**Ci**) Representative time series for clusters related to stationarity. (**Cii**) Representative time series for clusters related to micro movements and walking initiations. (**D**) First transition mode from the SVD factorization of the one-step transition probability matrix.

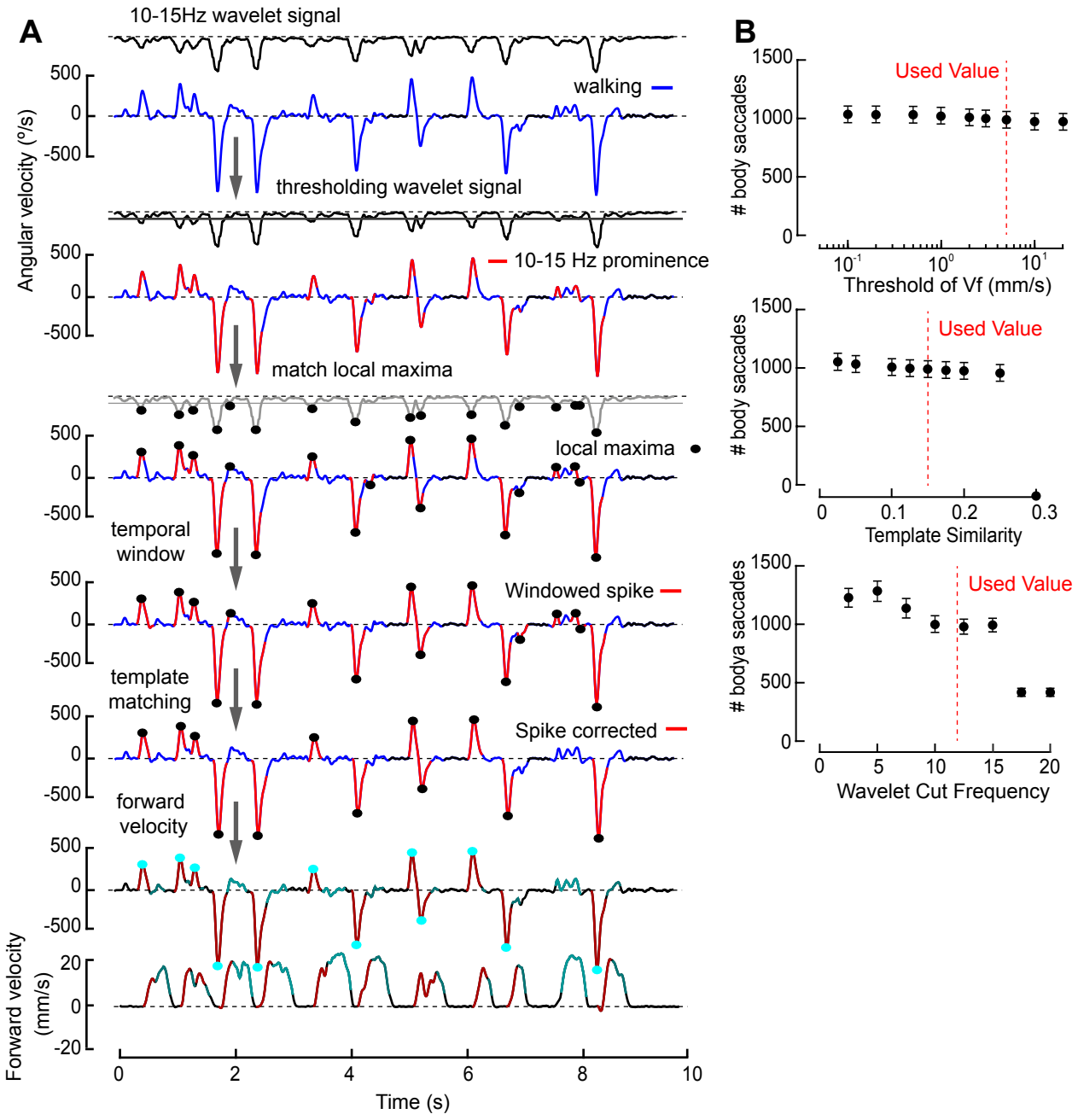

Figure S3: Body saccade supervised detection heuristics, related to Figure 3. (**A**) Different steps involved in the identification of rapid spikes of angular velocity that are referred to as body saccades in this study. See **Methods** for a full description of each step. (**B**) Exploration of the parameter space of the body saccade detection heuristics. Top, the number of body saccades using different thresholds for the forward speed (Vf) reduction during a body saccade in light and dark conditions. Middle, the number of body saccades using different thresholds for the template matching during a body saccade in light and dark conditions. Bottom, the number of body saccades using different wavelet frequency cuts for the putative body saccades in light and dark conditions. For all the sets of heuristic parameters used, the variations in the number of body saccades were generally small and did not affect the differences between experimental conditions.

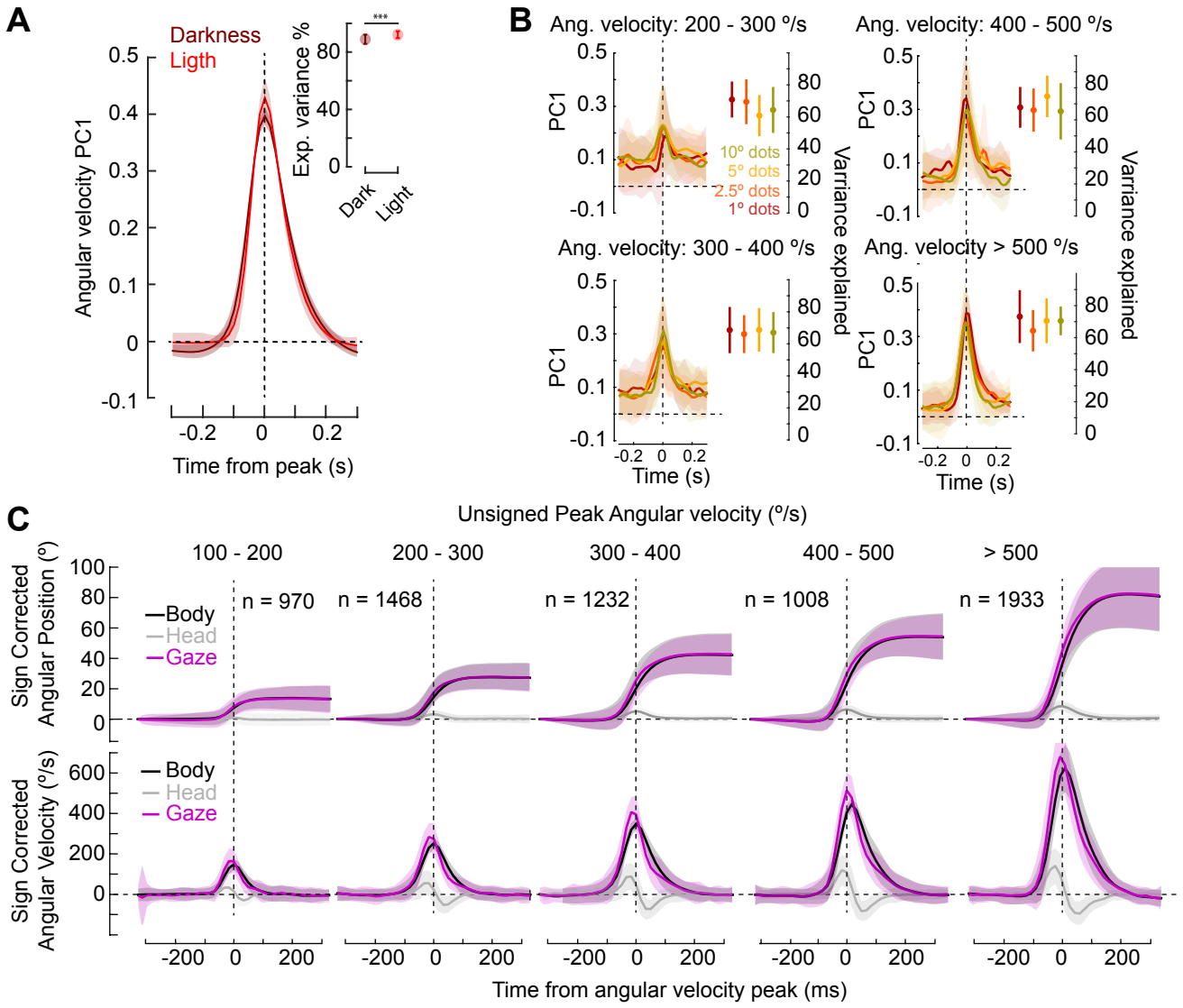

Figure S4: Head-body coordination during body saccades, related to Figure 3. A) Dynamics of the first principal component of the angular velocity during body saccades (variance explained > 90%, inset), in light (N = 33, n = 1022) and dark (N = 24, n = 4252) conditions. (**B**) Dynamics of the first principal component of the head movement during body saccades (variance explained ~70%), under various visual conditions and for different amplitudes of the body saccade. (**C**) Top: time series of the angular displacement of the body, head and gaze during body saccades of increasing amplitude. Bottom: time series of the angular velocity of the body, head and gaze during body saccades of increasing amplitude.

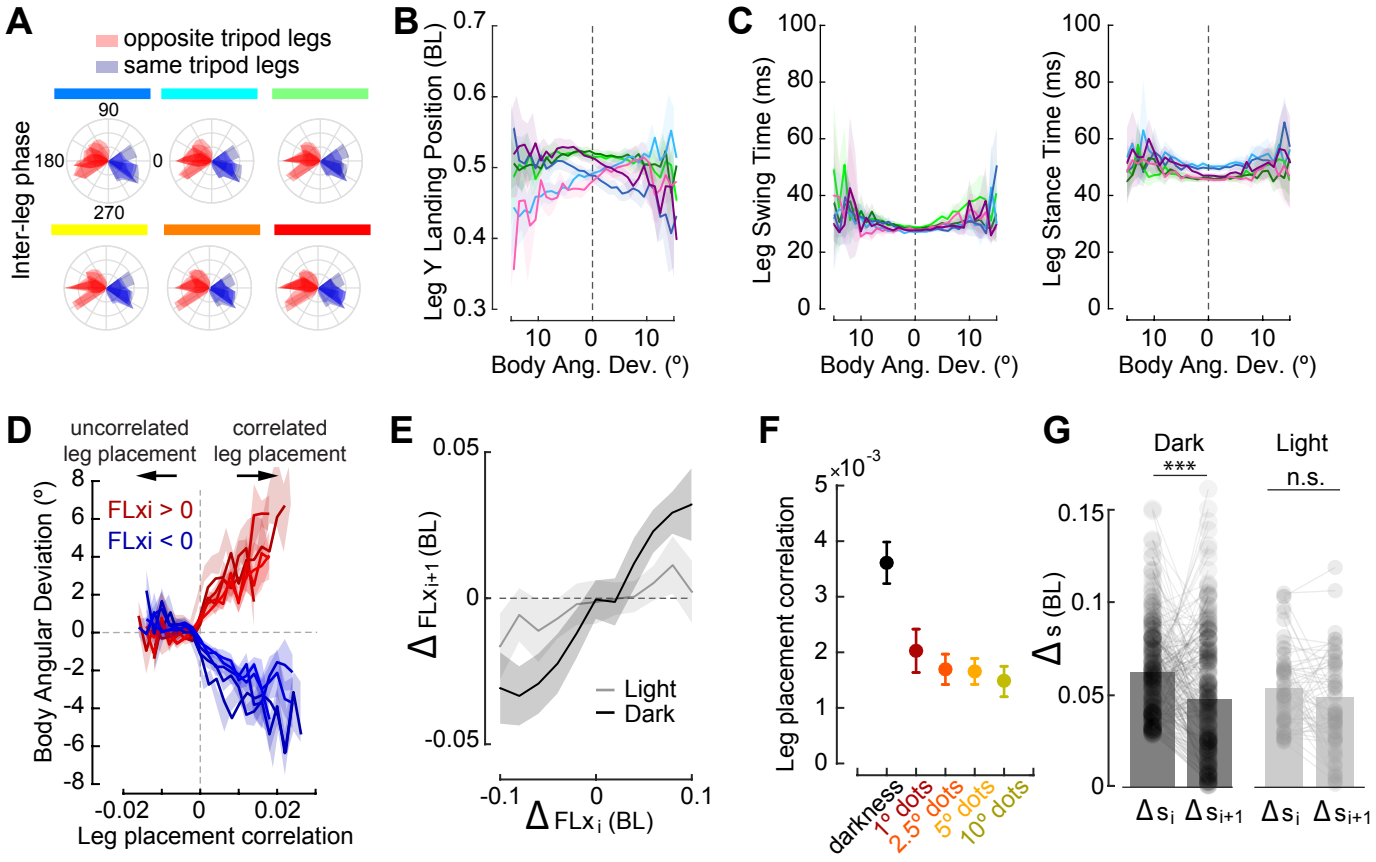

Figure S5: Leg movements during forward runs, related to Figure 5. (**A**) Inter-leg phase as a function of deviation from straight path during forward runs. Blue shades: leg phases between legs belonging to the same tripod, red shades: leg phases between legs belonging to opposite tripods (N = 52 flies, n = 15754 forw. runs). (**B**) Leg Y landing position in a single step as a function of the body angular deviations detected in that step. Individual legs follow the color code shown in **Figure 5A**. (N = 52 flies, n = 42524 high quality steps) (**C**) Leg swing and stance time in a single step as a function of the body angular deviations detected in that step. (N = 52 flies, n = 42524 high quality steps) (**D**) Body angular deviations as a function of the correlated lateral movement of both front legs divided by the direction of the initial lateral movement (red: rightward, blue: leftward) and the visual environment (different shades). (**E**) Front leg X landing position as a function of the contralateral front leg X landing position in the preceding step for darkness (black) or 10º dots (gray) conditions. (**F**) Average front leg placement correlation in different visual conditions (N = 52, n = 42524 high quality steps). (**G**) Change in postural stability in consecutive steps under darkness (left, N = 24, n= 620 high quality steps) or 10º dots (right, N = 28, n = 2222 high quality steps) conditions (*** p<0.005, Wilcoxon signed-rank test).

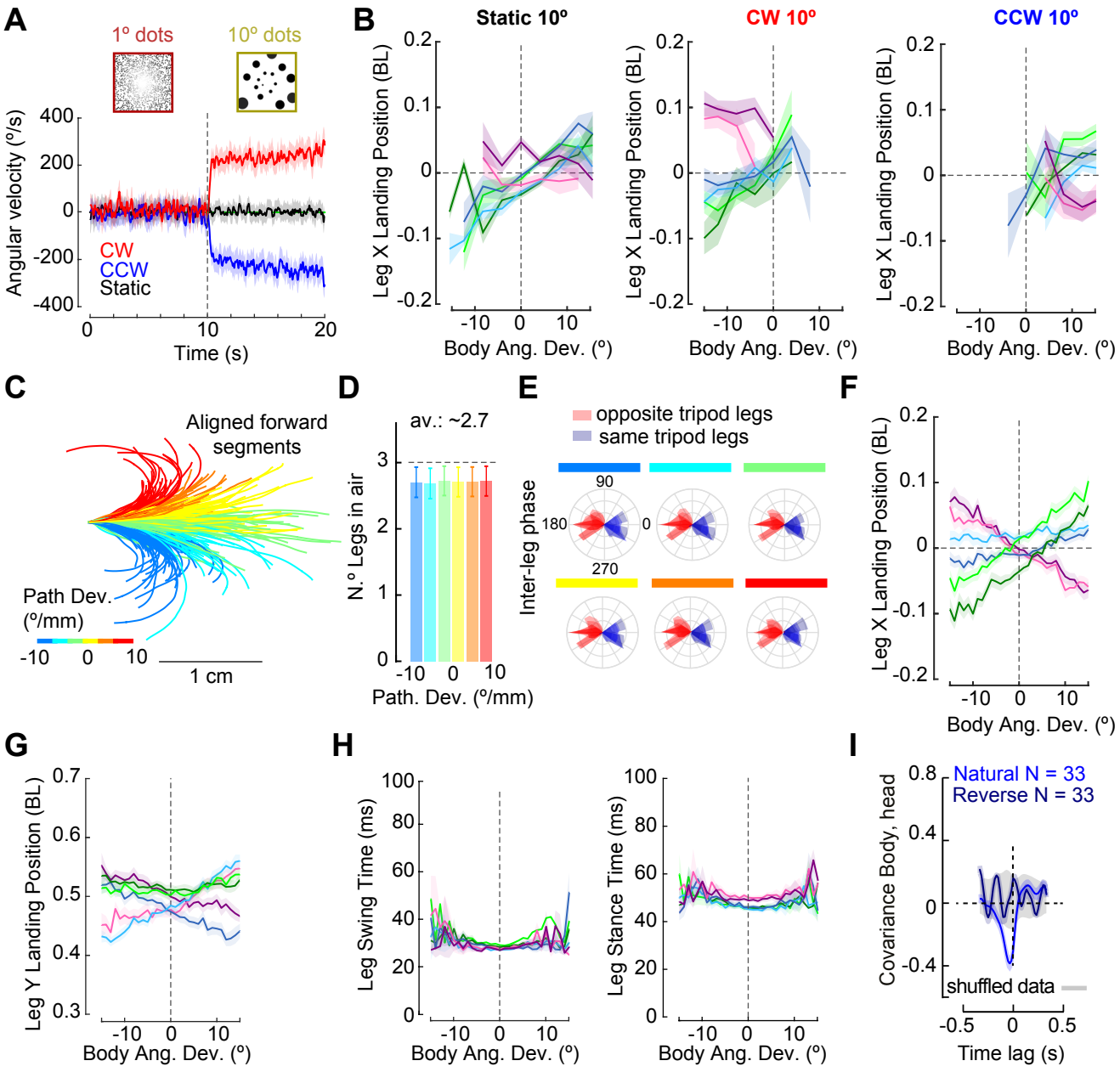

Figure S6. Leg movements during forward walking under external visual perturbations, related to Figure 5. (**A**) Average angular velocity under different open-loop rotations of the visual environment (red: clockwise visual rotation, CW; blue: counterclockwise visual rotation, CCW; black: static visual stimuli) for 1º dots and 10º dots. (**B**) Leg X landing position in a single step in a OMR paradigm as a function of the body angular deviations detected in that step. Visual environment: 10º dots. Individual legs follow the color code shown in **Figure 5A**. Left: static stimuli, middle: CW visual rotation, right: CCW visual rotation. (**C**) Example set of forward segments during reversed gain conditions aligned to the starting position. Color code corresponds to the magnitude of the walking path's deviation during each segment. (**D**) Number of legs in the air at each frame during forward segments for different amounts of path deviation (N = 28, n = 11470 forward runs). A perfect tripod gait corresponds to 3 legs in the air at all times (dashed line). (**E**) Same as **Figure S5A** for forward runs under reversed gain. (**F**) Leg X landing position in a single step as a function of the body angular deviations detected in that step (N = 28, n = 22329 steps). Individual leg color code as in **A**. (**G**), (**H**) Same as **Figure S5B,C** for forward runs under reverse gain. (**I**) Head-body coordination measured as the cross-covariance between head angle and body angular velocity during forward runs in natural and reversed conditions. Gray: same as in (**Figure 3C**).

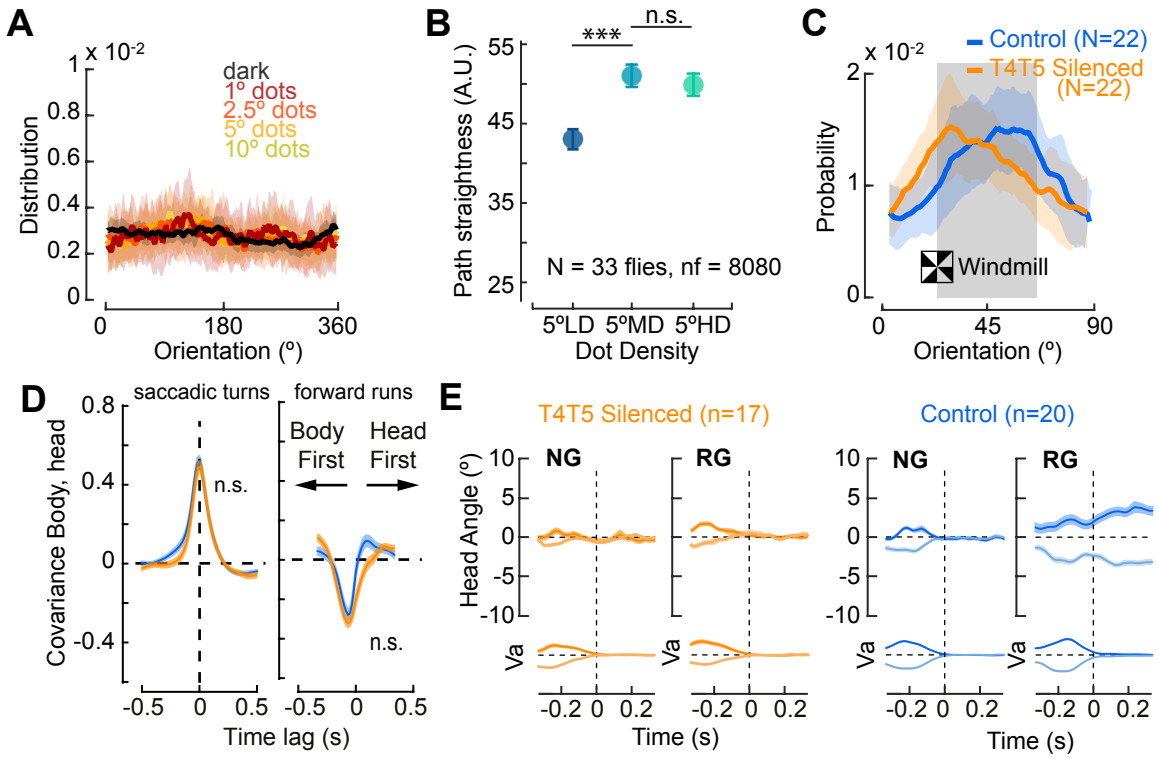

Figure S7. Evidence for spatial integration of visual motion signals on gaze fixation, related to Figure 6. (**A**) Orientation preference distribution under NG for different visual environments. (**B**) Straightness of forward runs as a function of dot density, MWWTest, *p<0.05, **p<0.01, ***p<0.005. (**C**) Probability of the orientation of a walking fly with respect to a black 45º bar. Bars are presented as a windmill visual environment under NG. Blue: control flies; orange: T4/T5 silenced flies. T4T5 silenced preference is shifted to one edge. (**D**) Head-body coordination measured as the cross-covariance between head angle and body angular velocity, during body saccades (left) or forward runs (right) in control (blue) and T4/T5 silenced flies (orange). (**E**) Head after-effects (see Methods) in control flies (right) and T4/T5 silenced flies (left) under NG and RG conditions. Events were separated for rightward (dark) and leftward (light) rotations before the fly stopped walking (dotted line).